Modeling of progressive high-cycle fatigue in composite laminates accounting for local stress ratios

Hofman, P.; van der Meer, F.P.; Sluys, Lambertus J.

Important note
To cite this publication, please use the final published version (if applicable).
Please check the document version above.

Modeling of progressive high-cycle fatigue in composite laminates accounting for local stress ratios

P. Hofman *, F.P. van der Meer, L.J. Sluys

Delft University of Technology, Delft, Netherlands

ARTICLE INFO

ABSTRACT

A numerical framework for simulating progressive failure under high-cycle fatigue loading is validated against experiments of composite quasi-isotropic open-hole laminates. Transverse matrix cracking and delamination are modeled with a mixed-mode fatigue cohesive zone model, covering crack initiation and propagation. Furthermore, XFEM is used for simulating transverse matrix cracks and splits at arbitrary locations. An adaptive cycle jump approach is employed for efficiently simulating high-cycle fatigue while accounting for local stress ratio variations in the presence of thermal residual stresses. The cycle jump scheme is integrated in the XFEM framework, where the local stress ratio is used to determine the insertion of cracks and to propagate fatigue damage. The fatigue cohesive zone model is based on S-N curves and requires static material properties and only a few fatigue parameters, calibrated on simple fracture testing specimens. The simulations demonstrate a good correspondence with experiments in terms of fatigue life and damage evolution.

1. Introduction

Fiber reinforced polymer (FRP) composites have many advantages over traditional (metallic) engineering materials and are increasingly used in the aerospace and automotive industries. These materials possess high-strength-to-weight ratios, good corrosion resistance and the material can be tailored to meet specific requirements by altering the stacking-sequence, fiber material, matrix material and ply thickness.

In order to speed-up and improve the design and certification process of FRP laminated structures, numerical models must be developed to predict the behavior under critical loading conditions. Cyclic loading is an important loading condition and is often governing for the design of composite structures.

In previous years, many high-cycle fatigue models have been developed, capable of accurately simulating fatigue crack growth in specimens with pre-existing cracks [1–13]. However, there are still challenges in progressive fatigue modeling of multidirectional laminates, where both intra- and inter-laminar cracks can initiate, propagate and interact and the final failure mode is a combination of multiple complex failure processes [14–17].

A few authors have developed a progressive failure modeling methodology to predict fatigue failure in composite laminates [18–25]. In most of the methods, Paris-type fatigue cohesive zone models are used to describe fatigue crack propagation, while fatigue crack initiation is simulated with criteria based on S-N curves. Therefore, these two stages of fatigue damage are treated separately and a large

amount of material characterization tests is required to obtain Paris' and S-N curves for different mode-mixities and stress ratios.

Recently, Dávila [26–28] proposed a fatigue cohesive zone model, covering fatigue crack initiation and propagation in a unified formulation. The model requires the static material properties and a limited number of fatigue parameters that can be obtained by calibration with typical fracture characterization tests. The effects of mode-mixity and stress ratio are taken into account in the constitutive equations through empirical relations and engineering assumptions. The fatigue cohesive zone model has been validated against simple fracture tests with thermosets [26–30], tests exhibiting $\mathcal{R}$-curve effects with thermoplastics [31], a *reinforced double cantilever beam* specimen with changing crack front shapes [29,32] and a *clamped tapered beam* specimen with delamination-migration [33]. Furthermore, the model successfully predicted initiation of transverse matrix cracks in $[0_2/90_4]_s$-laminates with thermal residual stresses [34]. Recently, the model has been used to simulate progressive fatigue failure in an open-hole $[0/90]_s$-laminate with predefined splits [25] and in an open-hole $[\pm 45]_s$-laminate with multiple transverse matrix cracks using XFEM [35]. However, the applicability of the fatigue cohesive zone model to simulate progressive failure in quasi-isotropic open-hole laminates with a complex interaction of distributed transverse matrix cracks and delamination has not yet been demonstrated.

Moreover, most of the progressive fatigue failure models employ predefined discrete cracks to simulate transverse matrix cracks and
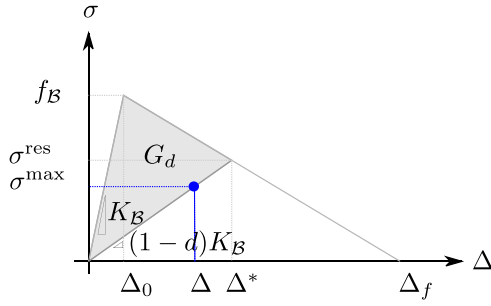
Fig. 1. Fatigue cohesive zone model: the traction-separation response under fatigue loading (•) is inside the quasi-static envelope.

splits [18,20,23,25], or a continuum damage mechanics model in combination with fiber-aligned meshes [24]. With XFEM, fiber-aligned meshes are not required and unstructured meshes can be used, thereby reducing meshing efforts. Furthermore, XFEM captures the discrete nature of a transverse (mesoscale) crack and allows for multiple cracks at arbitrary locations, which makes it possible to simulate the complete failure process from distributed cracking to localized failure, including the interaction between discrete matrix cracks and delamination.

This paper builds on previous work [35], where a robust and efficient XFEM-based progressive failure framework for tensile static loading [36,37] has been extended for simulating high-cycle fatigue. In this framework, both intra- and inter-laminar cracking are modeled with Dávila's mixed-mode fatigue cohesive zone model for simulating fatigue crack initiation and propagation with only a few input parameters. Furthermore, the fatigue cohesive zone model has been enhanced with an implicit time integration scheme of the damage variable and a fully consistent tangent to improve efficiency of the full-laminate analyses. The progressive fatigue failure framework is further extended in this work by using an adaptive cycle jump strategy that can capture local stress ratios. This is particularly important in multidirectional laminates, where due to the presence of non-uniform thermal residual stresses after curing, the local stress ratio varies in the laminate. Simulations of two quasi-isotropic open-hole laminates, with different stacking sequences, are performed with various tensile cyclic loadings and results are compared against experimental data from literature.

This paper is organized as follows. First, the fatigue cohesive zone model with implicit fatigue damage update is summarized, followed by the formulation of XFEM for simulating intra-laminar cracking. Then, the extension with an efficient adaptive cycle jump scheme for simulating high-cycle fatigue, while accounting for local stress ratios, is addressed. Finally, the simulation results of two quasi-isotropic open-hole laminates are presented and discussed.

2. Progressive failure framework

2.1. Fatigue cohesive zone model

The high-cycle fatigue cohesive zone model by Dávila [26] builds upon Turon's static mixed-mode cohesive zone model [38–40] and is formulated in terms of an equivalent 1D traction-separation relation:

$$\sigma = (1 - d)K_{\mathcal{B}}\Delta \tag{1}$$

where σ is the equivalent traction, $K_{\mathcal{B}}$ is the mode-dependent dummy stiffness and Δ is the equivalent displacement jump (see Fig. 1).

The damage variable d is related to an energy-based damage variable $\mathcal{D}$, defined as the ratio of dissipated energy G_d over the critical mixed-mode energy release rate G_c

$$\mathcal{D} \equiv \frac{G_d}{G_c} = \frac{\Delta^* - \Delta_0}{\Delta_f - \Delta_0} \tag{2}$$

where Δ_0 and Δ_f are the initiation and ultimate equivalent displacements, respectively. Furthermore, the reference displacement (corresponding to the displacement at which static damage develops) is defined as

$$\Delta^* = \mathcal{D}(\Delta_f - \Delta_0) + \Delta_0 \tag{3}$$

The energy-based damage variable $\mathcal{D}$ is the state variable and can only increase in *pseudo* time t, such that for current time step t_n

$$\mathcal{D}(t_n) = \max_{0 \leq \tau \leq t_n} \left(\mathcal{D}(\tau) \right) \tag{4}$$

The stiffness-based damage variable d in Eq. (1) is related to the energy-based damage variable with the following equation

$$d = 1 - \frac{(1 - \mathcal{D})\Delta_0}{\mathcal{D}\Delta_f + (1 - \mathcal{D})\Delta_0} \tag{5}$$

The evolution of the energy-based damage variable is such that, at constant stress amplitudes and mode-mixities, the number of cycles to failure is described by an S-N curve (see Fig. 2). The rate of change of the damage variable $\mathrm{d}\mathcal{D}/\mathrm{d}N$ is described with a nonlinear differential equation

$$\frac{\mathrm{d}\mathcal{D}}{\mathrm{d}N} = \frac{1}{\gamma} \frac{(1 - \mathcal{D})^{\beta-p}}{E^\beta(p+1)} \left(\frac{\Delta}{\Delta^*} \right)^\beta \tag{6}$$

where the right-hand side is the CF20 damage accumulation function [27]. In this function, γ is the number of cycles to failure at the endurance limit, p can be calibrated to Paris curves and β is the exponent in the S-N curve, expressed as

$$\beta = \frac{-7\eta}{\log E} \tag{7}$$

where η is a *brittleness* parameter to account for the low-cycle fatigue response. For a given stress ratio R, the relative endurance limit E, defined as the ratio of equivalent endurance limit σ_{end} and mode-dependent static strength $f_{\mathcal{B}}$, is computed from the endurance limit ϵ at full load reversal ($R = -1$) with the Goodman diagram:

$$E = \frac{2C_1\epsilon}{C_1\epsilon + 1 + R(C_1\epsilon - 1)} \tag{8}$$

In this expression, C_1 is an empirical relation which accounts for the effect of mode-mixity [41]

$$C_1 = 1 - 0.42\mathcal{B} \tag{9}$$

where $\mathcal{B}$ is a displacement-based measure for mode-mixity and is defined as

$$\mathcal{B} = \frac{K_{sh}[\![u]\!]_{sh}^2}{K_n \langle [\![u]\!]_n \rangle^2 + K_{sh}[\![u]\!]_{sh}^2} \tag{10}$$

which is a function of the normal and shear dummy stiffnessess (K_n and K_{sh}) and the normal and shear displacement jumps ($[\![u]\!]_n$ and $[\![u]\!]_{sh}$). Furthermore, the ratio of shear and normal stiffness must satisfy the constraint equation in Ref. [39] to ensure correct energy dissipation during static mixed-mode fracture.

Following the previous work [35], the fatigue damage at current *pseudo* time t_n is computed with an implicit time integration scheme, using the trapezoidal rule:

$$\mathcal{D}_f^{(n)} = \mathcal{D}^{(n-1)} + \frac{\Delta N}{2} \left(\frac{\mathrm{d}\mathcal{D}}{\mathrm{d}N}^{(n-1)} + \frac{\mathrm{d}\mathcal{D}}{\mathrm{d}N}^{(n)} \right) \tag{11}$$

where the damage rates $\mathrm{d}\mathcal{D}/\mathrm{d}N^{(n-1)}$ and $\mathrm{d}\mathcal{D}/\mathrm{d}N^{(n)}$ are determined by evaluating Eq. (6) with values of the previous and the current *pseudo* time step, respectively. This nonlinear equation is iteratively solved at *local* integration point level with Newton's method. The quasi-static damage $\mathcal{D}_s$ is computed as

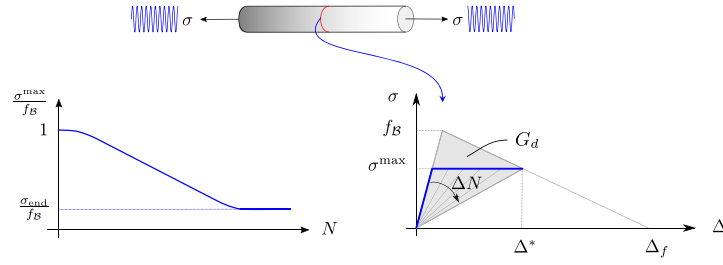$$\mathcal{D}_s = \frac{\Delta - \Delta_0}{\Delta_f - \Delta_0} \tag{12}$$

Fig. 2. S-N-based fatigue cohesive zone model.

and the updated damage is determined as the maximum of the static and the fatigue damage

$$D = \max(D_s, D_f) \tag{13}$$

The formulation is completed with a consistent tangent stiffness matrix, which is derived and presented in Ref. [35].

2.2. Intra-laminar cracking

The *phantom node version* of XFEM [42] is used for simulating distributed matrix cracks at arbitrary locations [36,37,43]. A crack segment is inserted in a continuum element as soon as the stress in the plies σ reaches a critical envelope $f_I(\sigma) = 1$. The discontinuity in the displacement field is resolved by duplicating the original element and defining the connectivity of each sub-element Ω_A and Ω_B (see Fig. 3) as

$$\Omega_A^{\text{conn}} = \{\tilde{n}_1, \tilde{n}_2, n_3\} \tag{14}$$

$$\Omega_B^{\text{conn}} = \{n_1, n_2, \tilde{n}_3\} \tag{15}$$

where $\{n_i\}$ and $\{\tilde{n}_i\}$ are the set of original and *phantom* nodes, respectively.

The displacement field of the XFEM element is expressed in terms of the independent displacement fields of the two sub-elements that are overlapping:

$$\mathbf{u}(\mathbf{x}) = \begin{cases} \mathbf{N}(\mathbf{x})\mathbf{u}_A, & \mathbf{x} \in \Omega_A \\ \mathbf{N}(\mathbf{x})\mathbf{u}_B, & \mathbf{x} \in \Omega_B \end{cases} \tag{16}$$

where $\mathbf{u}_A$ and $\mathbf{u}_B$ are the vectors with nodal degrees of freedom of each sub-element and $\mathbf{N}(\mathbf{x})$ is the matrix containing the shape functions. The displacement jump vector along the crack segment Γ_d is defined as

$$[\![\mathbf{u}]\!](\mathbf{x}) = \mathbf{N}(\mathbf{x})(\mathbf{u}_A - \mathbf{u}_B), \quad \mathbf{x} \in \Gamma_d \tag{17}$$

The crack segment is inserted parallel to the direction of the fibers in the ply to enforce transverse cracks to propagate in fiber direction. The traction-separation relation of the cohesive integration points that are located on the crack segment is described by the fatigue cohesive zone model (Section 2.1).

In order to retain well-posedness of the problem, a predefined crack-spacing parameter l_c is used [36]. XFEM crack segments can be inserted either at zero orthogonal distance of existing cracks (propagation), or initiate as new cracks at a distance that is at least equal to l_c. The objectivity of the crack-spacing parameter is discussed in earlier publications for static loading [37] and for fatigue loading [35].

XFEM crack segments are inserted when a fatigue crack insertion criterion ($f_I(\sigma) > 1.0$) is satisfied. The criterion is based on the endurance limit to maintain consistency with the fatigue damage formulation [35]. The failure index function is defined as the ratio of the equivalent traction σ to the endurance limit σ_{end}:

$$f_I(\sigma) \equiv \frac{\sigma(\sigma)}{\sigma_{\text{end}}(\sigma)} \tag{18}$$

with $\sigma_{\text{end}} = E f_B$. The relative endurance limit E is determined from Eqs. (8) and (9) and the mode-dependent static strength f_B is computed as

$$f_B = \sqrt{(K_n(1-B) + BK_{sh})\left[f_n^2/K_n + (f_{sh}^2/K_{sh} - f_n^2/K_n)B^\eta\right]} \tag{19}$$

where f_n and f_{sh} are the normal and shear static strengths. During the static ramp-up phase and the control cycles (see Section 2.3), fatigue damage is inactive ($R = 1$) and a static criterion is used with failure index function:

$$f_I(\sigma) = \frac{\sigma(\sigma)}{f_B} \tag{20}$$

2.3. Cycle jump scheme

A cycle jump approach, which takes into account the effects of the cyclic load in the constitutive relation, is often used in high-cycle fatigue analyses since simulating each cycle explicitly would be computationally intractable. A load envelope approach can be used to apply the loading in a simplified way, for example when a constant amplitude cyclic load is applied and all inelastic behavior is assumed to be of damage-type (with secant unloading), which makes the unloading-reloading a linear problem. Because of this linearity, the *global* load ratio is equal to the *local* stress ratio in each integration point. Consequently, the *local* stress ratio is *a priori* known and can be provided as an input parameter of the constitutive equations. This approach is used by many authors for the simulation of high-cycle fatigue [1–13,26,27,33,44,45].

In the presence of multiple unsynchronized load signals, plasticity, geometric nonlinearities or thermal residual stresses, the *local* stress ratio is not equal to the *global* load ratio. However, the load envelope approach does not give access to the *local* stress ratios, even though these should govern the *local* material response.

One approach to overcome this issue is to use a *min–max* technique [46], where two models, one with the minimum and the other with the maximum applied load, are used and information is exchanged between them. Another, more general approach, is a cycle jump strategy with explicit load cycles, also called *control cycles*, before each cycle increment ΔN, as previously applied to composite materials by various authors [34,47–50]. During these control cycles, the minimum and maximum stresses are monitored such that after the control cycle, the *local* stress ratio can be computed before a cycle jump ΔN is applied. During the cycle jump, the *local* stress ratio is then available for use in the calculation of fatigue damage.

Joosten et al. [34] combined this cycle jump approach with Dávila's fatigue CZM and proposed a *local* stress ratio definition, computed during the control cycles with a projection of the minimum and maximum severities:

$$R \equiv \frac{\mathbf{S}_{\text{min}} \cdot \mathbf{S}_{\text{max}}}{\|\mathbf{S}_{\text{max}}\|^2} \tag{21}$$

where $\mathbf{S} = \left[t_n/f_n, t_{sh}/f_{sh}\right]^{\mathrm{T}}$ is the stress severity vector. The components of this vector contain the normal (t_n) and shear traction (t_{sh}) components, scaled with the pure-mode strengths.
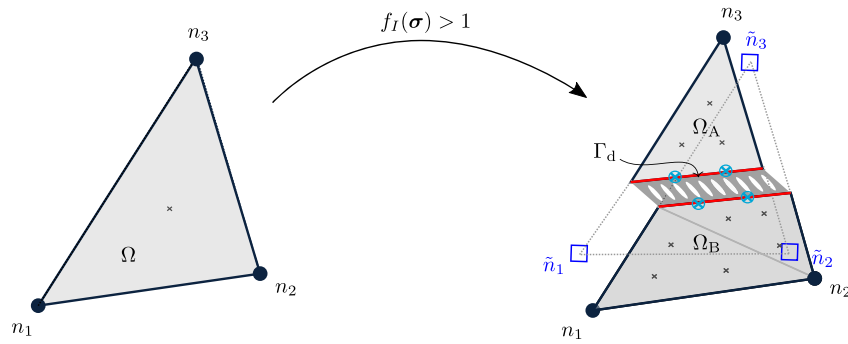
Fig. 3. XFEM crack insertion. The mixed-mode fatigue cohesive zone model is used in each cohesive integration point ($\otimes$) for describing fatigue damage.
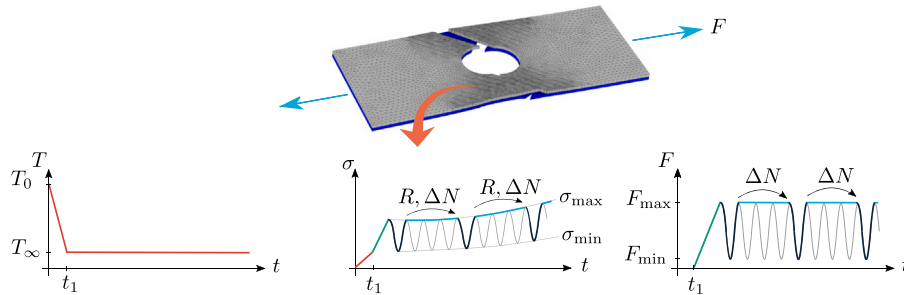

Fig. 4. Cycle jump scheme with four phases: thermal load phase (in *red*), static ramp-up phase (in *green*), control cycle phase (in *dark blue*) and cycle jump phase (in *light blue*).

In this work, a similar approach is followed to capture the varying *local* stress ratio in quasi-isotropic laminates with non-uniform thermal residual stresses. Four different loading phases are defined. First, a *thermal load phase* is applied to simulate a temperature drop from the curing temperature T_0 to the cooling temperature T_∞, resulting in a residual stress in every material point due to the mismatch of thermal constants between plies. After the thermal load phase, the *static-ramp-up phase* is simulated to reach the maximum load $F_{\max}$. Subsequently, a *control cycle* is applied in order to determine the *local* stress ratio in every integration point. When the control cycle has finished, a *cycle jump phase* is entered in which fatigue damage accumulates according to the formulation with *local R* in Eq. (8). After each cycle jump phase, a control cycle is re-entered to update the stress ratios for the next cycle jump phase. This process is repeated until all fatigue cycles have been simulated. An overview of these phases is shown in Fig. 4.

Remark. It should be mentioned that the use of control cycles to compute the *local* stress ratio in each integration point is an explicit procedure. Since fatigue damage accumulates during cycle jumps, resulting in stress redistribution in the laminate, the *local* stress ratio that is used at the beginning of the step is different from the *local* stress ratio at the end of the step. Although time step dependence has been reduced strongly with the implicit time integration scheme [35], a re-assessment of the time step dependence is required. This is carried out in the numerical examples later in this article (Section 3.2.2).

2.4. Monitoring the local stress ratio in the bulk integration points

At the end of each cycle jump, the failure index function Eq. (18) must be evaluated in every integration point. For this purpose, the *local* stress ratio must be available for computing the endurance limit with Eq. (8). The local stress ratio in Eq. (21) is defined with traction components in local coordinate frame, aligned with the crack segment. Since crack segments are inserted parallel to the fiber direction, the traction vector $\mathbf{t}$ can be computed from the bulk stress σ and the normal vector $\mathbf{n}$, that is perpendicular to the fibers, with $\mathbf{t} = \sigma\mathbf{n}$. The *local* stress ratio can then be computed during control cycles in each bulk integration point, such that it is available when Eq. (18) is evaluated.

2.5. Transferring local stress ratio from bulk to cohesive integration points

Once new crack segments are inserted, the solution must be re-equilibrated by re-entering the Newton–Raphson solver. Upon insertion of new crack segments, the *local* stress ratio R must be known to evaluate fatigue damage in each new cohesive integration point. To achieve this, the bulk *local* stress ratio is passed to the cohesive integration points on the newly inserted crack segments. With linear (constant stress) elements, this is straightforward. With other types of elements where the stress, and thus the *local* stress ratio, varies across an element, the history transfer approach by Wells and Sluys [51] is a suitable method.

2.6. Adaptive stepping strategy

Since an implicit time integration scheme is employed for updating the fatigue damage variable during cycle jumps, the cycle increment ΔN can be determined based on *global* convergence behavior [35]. An adaptive stepping scheme is used during each loading phase of the analysis. The number of iterations n_{iter}, required to reach convergence in the previous time step, is used to determine the next step size:

$$\Delta t^{(n+1)} = C^{-\left(\frac{n_{\text{iter}} - n_{\text{iter}}^{\text{opt}}}{\xi}\right)} \Delta t^{(n)} \tag{22}$$

where C, ξ and $n_{\text{iter}}^{\text{opt}}$ are model parameters and Δt is an increment in *pseudo* time which translates to a cycle increment during cycle jumps and to a load increment during static ramp up and control cycles. If convergence is not reached within a specified maximum number of iterations $n_{\text{iter}}^{\max}$, the step is cancelled and restarted with a reduced time step increment $\Delta t^{(n)} \leftarrow c_{\text{red}} \Delta t^{(n)}$.

At the start of the first cycle jump, the step size ΔN_{init} is initialized and used to compute fatigue damage. This step size is adapted during the subsequent cycle jumps according to Eq. (22). After the cycle jump phase and before a new control-phase is entered, the new cycle increment ΔN is computed and stored as the initial cycle increment for the next cycle jump phase. This ensures that the control cycle increments and the cycle jumps are separately adapted.
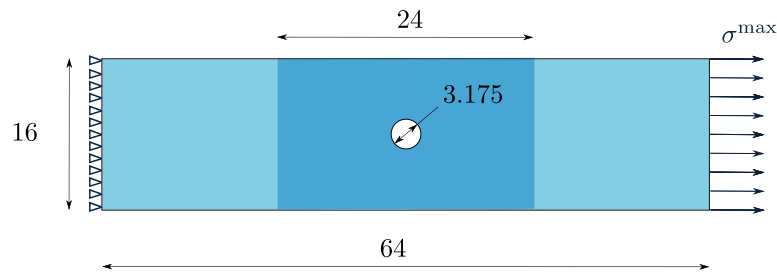
Fig. 5. Specimen dimensions (in mm) of the quasi-isotropic open-hole laminates. The fine mesh region is indicated in dark blue.

Table 1
Ply material properties used in the simulations.

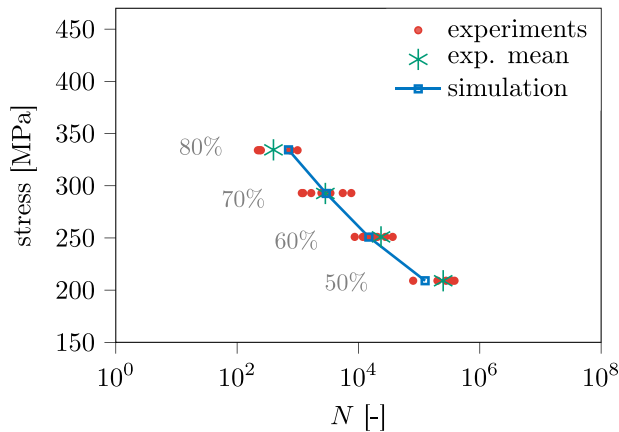| elastic [52]		fracture [53]		fatigue [27]		thermal [52]	
E_1	161.0 GPa	f_n	95 MPa	η	0.95	α_1	0 °C^{-1}
E_2	11.38 GPa	f_s	107 MPa	ϵ	0.2	α_2	3.0×10^{-5} °C^{-1}
G_{12}	5.17 GPa	G_{Ic}	1.0 N mm^{-1}	p	β		
ν_{12}	0.32	G_{IIc}	1.0 N mm^{-1}				
		η	2.1				

Fig. 6. S-N curve of the ply-level scaled specimen.
Source: Experimental values are extracted from [16].

When control cycles are entered, it is first tried to find the solution at the minimum load at once. Since fatigue damage is de-activated during control cycles and the analysis reduces to a linear problem, only two steps, corresponding to the minimum and maximum load, are sufficient in most cases. Sometimes, more steps during control cycles are necessary, in which case the time step is adapted as described above.

2.7. Modeling thermal residual stresses

Multidirectional laminates develop residual stresses after curing due to a mismatch in thermal constants between plies. The effect of a temperature change ΔT is taken into account in the ply constitutive model. The orthotropic linear elastic stress–strain relation in 2D is

$$\boldsymbol{\sigma} = \mathbf{D}(\boldsymbol{\epsilon} - \boldsymbol{\epsilon}^{th}) \tag{23}$$

where

$$\boldsymbol{\epsilon}^{th} = \left[\alpha_1 \Delta T, \alpha_2 \Delta T, 0\right]^T \tag{24}$$

is the thermal strain, with α_i the coefficients of thermal expansion in longitudinal (fiber) direction (α_1) and in transverse direction (α_2).

3. Quasi-isotropic open-hole laminate simulations

Two quasi-isotropic open-hole laminates, experimentally tested in Refs. [15,16], have been simulated and results are presented in this

section. The laminates have the same number of plies and thicknesses but different lay-ups, leading to distinct failure modes and fatigue lifes. The first laminate has lay-up $\left[45_2/90_2/-45_2/0_2\right]_s$ and is *ply-level scaled*, where two plies with the same fiber direction are stacked, effectively increasing the ply thickness. The second laminate has lay-up $\left[45/90/-45/0\right]_{2s}$ and is *sub-laminate scaled*, in which the laminate is created by repeating *sub-laminates*. In the following, the first laminate is denoted as *ply-level scaled specimen* and the second as *sub-laminate scaled specimen*.

3.1. Model preliminaries

The open-hole laminates are made of carbon fiber/epoxy plies (prepreg system IM7/8552). The dimensions of the specimens are 64 mm × 16 mm × 2 mm with a hole diameter of 3.175 mm (see Fig. 5). The thickness of each ply is 0.125 mm. Thermal residual stresses arise by accounting for the temperature change ΔT from processing temperature (180 °C) to room temperature (20 °C) in the linear elastic constitutive relation (Section 2.7), while deformations are freely allowed to occur.

The static versions of these cases, experimentally tested in Ref. [54], were previously simulated with the same XFEM progressive failure framework for static loading [53], where the interface strength was reduced to 45 MPa, while the ply fracture energy in mode-I was increased to the value of mode-II, resulting in larger cohesive zone lengths and improved robustness while retaining a good fit with experimental measurements. In the present fatigue simulations, unadapted values for these parameters again gave rise to convergence problems and therefore the same set of static material properties as in Ref. [53] is used for this manuscript (see Table 1). For the fatigue-related parameters of CF20, recommended values are used from Ref. [27], which predicted excellent results with IM7/8552 carbon fiber/epoxy in a *double cantilever beam* test [26], *mixed-mode bending* test [33,34], *double notch shear* test [34], *clamped tapered beam* specimen [33] and $[0_2/90_4]_s$-laminate [34].

The dummy stiffness between the plies is related to the in-plane shear modulus and ply thickness t_p through $K_d = G_{12}/\frac{1}{2}t_p$ [37]. Furthermore, the crack-spacing parameter (see Section 2.2) is set to $l_c = 0.75$ mm. Since the lay-ups are symmetric, only half of each laminate is modeled. The computational domain is discretized with an unstructured mesh and each ply is represented by a layer of plane-stress, constant strain, triangular elements. A rectangular region around the hole is defined where delamination is allowed by inserting zero-thickness interface elements between the plies (shown in Fig. 5). This region has a fine-mesh with a typical element size of 0.4 mm. The typical element size outside this region is 1.6 mm, where the plies are rigidly tied. A Newton–Cotes integration scheme is used for the interface elements for superior interaction with the neighboring elements containing the transverse matrix cracks [37]. For the transverse matrix cracks in the plies, as well as for the plies themselves, Gauss integration schemes are used (see Fig. 3).

The adaptive stepping scheme in Section 2.6 allows for efficiently adapting the time steps in the static, control cycle, and cycle jump phases. Three cycle jumps are simulated in each cycle jump phase,
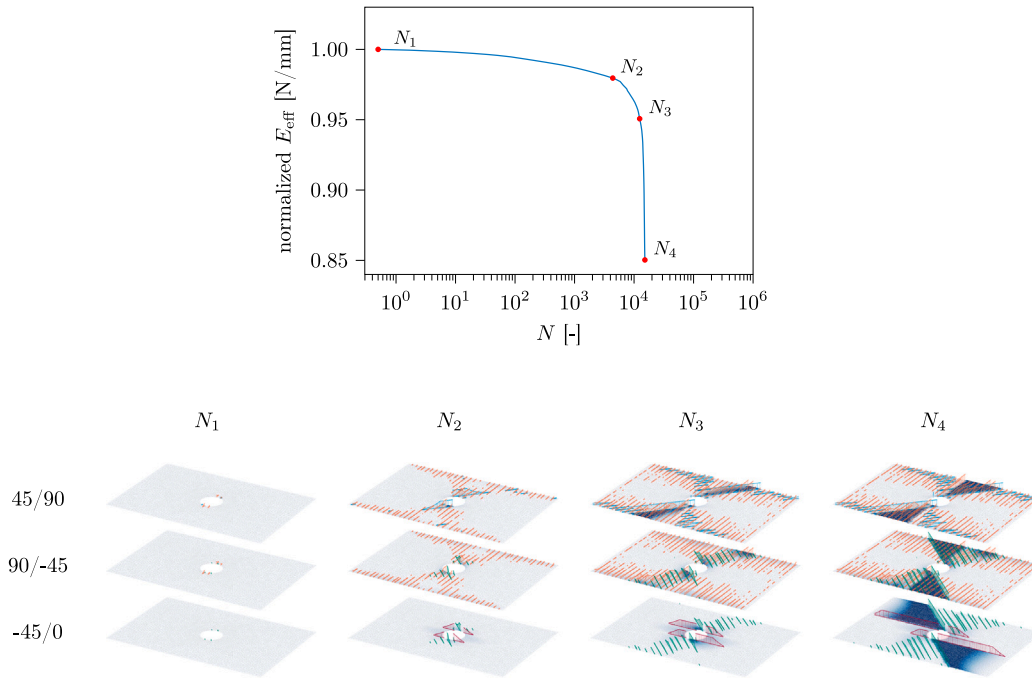
Fig. 7. Stiffness reduction as a function of number of cycles N (*top*) and damage evolution at indicated time instances in the interfaces (in *dark blue*) and XFEM matrix cracks in 45°-ply (in *light blue*), 90°-ply (in *orange*), −45°-ply (in *green*) and 0°-ply (in *red*).

after which a control phase is entered to update the *local* stress ratio in every integration point. The stepping parameters in Eq. (22) are set to $n_{\text{iter}}^{\text{opt}} = 4$, $C = 2$ and $\xi = 1$. The maximum number of iterations is set to $n_{\text{iter}}^{\text{max}} = 20$. If no convergence is obtained within $n_{\text{iter}}^{\text{max}}$, the step is restarted with a 40% reduction of the previous increment.

3.2. Ply-level scaled specimen

The *ply-level scaled specimen* is simulated with four different maximum applied stress levels $\sigma^{\text{max}}(\text{MPa}) = \{334.4, 292.6, 254.0, 209.0\}$, corresponding to 80, 70, 60 and 50% severity levels, respectively. Global severity is defined as the ratio of the maximum load over the static strength [15]. The *global* load ratio R_{glob} is 0.1.

3.2.1. Fatigue life and damage evolution

S-N curves from experiments and simulations are shown in Fig. 6, where the fatigue life corresponds to a 15% loss in normalized effective stiffness $E_{\text{eff}}/E_{\text{eff},0}$, associated with a steep drop in stiffness. The effective stiffness is computed consistently with the experiments as described in Ref. [16]. It can be observed that a good match is obtained with the experimental fatigue lifes. The stiffness reduction and evolution of fatigue damage in the interfaces for four different time instances are shown in Fig. 7. First, matrix cracks develop with a limited amount of stiffness loss, accompanied by delamination of small triangular areas near the hole (N_1 - N_2). A significant stiffness drop occurs due to delamination in the 45/90 interface, starting from the transverse matrix cracks (N_2 - N_3). When the matrix cracks have fully developed in the 90° and −45° plies, rapid delamination growth takes place in the 90/−45 and −45/0 interface, growing from the hole to the outer edges. This delamination corresponds to an almost vertical drop in the stiffness (N_3 - N_4). The final damage patterns at 15% stiffness reduction match well with the experimental damage patterns [15].

3.2.2. Efficiency and accuracy

The efficiency and accuracy of the simulations have been investigated. An implicit time integration scheme of the damage variable is used which allows for larger cycle increments. The combination of the implicit scheme and the consistent tangent enables the use of an adaptive time stepping strategy where the number of global iterations to reach a converged solution is a good measure to determine the cycle increment for the next *pseudo* time step [35].

The time step dependence (see remark in Section 2.3) and performance of the adaptive cycle jump scheme is assessed by repeating the 60% severity analysis with a small step size. This limits the amount of stress redistribution between steps and increases the number of control cycles with more regular updates of the *local* stress ratios. The maximum allowed cycle increment is set to $\Delta N = 10$ cycles.

The stiffness reduction curve is shown in Fig. 8 with markers for every individual time step, from which it can be observed that the global response in terms of stiffness degradation as function of number of cycles is very similar for the two simulations with 154 and 2746 time steps, respectively. The accumulation of the cycle number N with every time step is depicted in Fig. 9, which shows that the adaptive stepping strategy effectively adapts the cycle increments throughout the simulation.

It can be concluded that the adaptive stepping strategy, in combination with the implicit fatigue damage update and consistent tangent, results in efficient and accurate analyses resulting in relatively short run times (5834 s on a laptop computer[1]).

3.2.3. Effect of local stress ratio

In order to investigate the effect of accounting for the *local* stress ratio R, the analyses are repeated but this time with the *local* stress ratio in Eq. (8) set equal to the *global* load ratio $R_{\text{glob}} = F^{\text{min}}/F^{\text{max}} = 0.1$.

---

[1] Dell laptop with Intel Core i7 processor, 16 GB of RAM and operating system Linux Ubuntu 20.04.
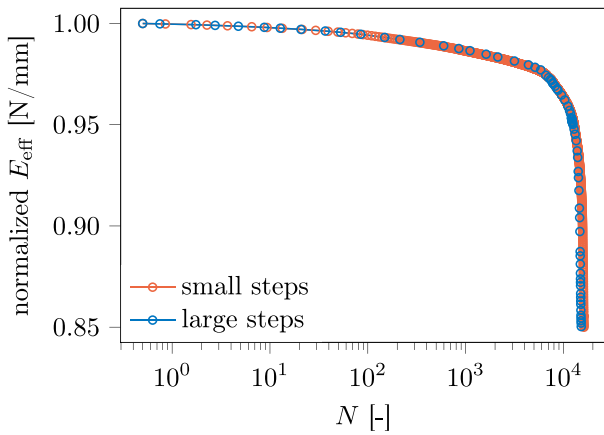
Fig. 8. Stiffness reduction with number of cycles.

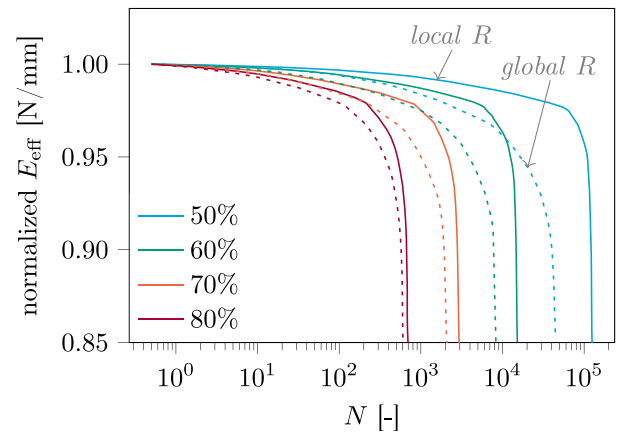**Fig. 9.** Accumulation of cycles with time steps.

Fig. 10. Stiffness reduction with number of cycles for four different severity levels. Dashed and solid lines correspond to the response with *global* and *local* stress ratio, respectively.
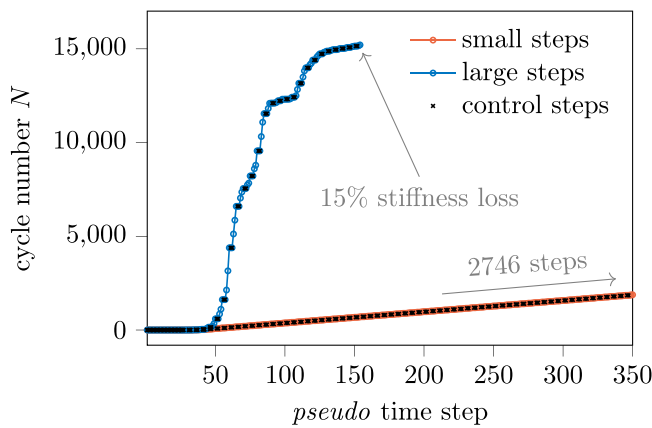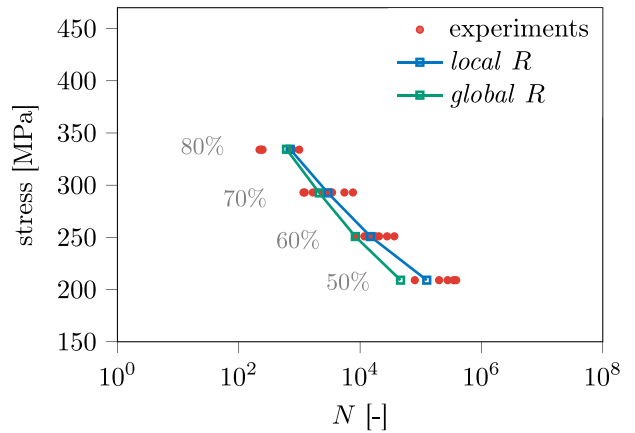

Fig. 11. S-N curve of the ply-level scaled specimen. *Local* stress ratio vs *global* load ratio.

The stiffness reduction curves with *global* and *local R* are shown in Fig. 10. It can be observed that accounting for *local* stress ratio results in a significantly slower development of fatigue damage. Furthermore, the use of the *local* stress ratio affects the slope of the laminate S-N curve, as shown in Fig. 11. The fatigue life prediction with the *global* load ratio shows a mismatch with the experimental values for the lower load levels, whereas with the highest load level, the response is almost independent of the use of *global* or *local R*.

In Fig. 12, the *local R* values in the cohesive zone (where $\mathcal{D} \in (0,1)$) are plotted as a field for the lowest (50%) and highest load level (80%) in every interface at approximately 7% stiffness loss. It can be observed that the *local* stress ratio is generally higher for the lowest load level, while for the highest load level the *local* stress ratio is close to the *global* load ratio. This can be explained by looking at Fig. 4, where the stress in a point is the superposition of the thermal residual stress and the stress due to the mechanical load. With an increased maximum load and equal *global* load ratio, the *local* stress ratio reduces due to the diminishing relative magnitude of the residual stresses.

With an overall larger stress ratio, fatigue damage accumulates slower compared to simulations in which a *global* load ratio is used in every integration point, leading to an increased discrepancy between the simulation results with decreasing maximum load level (Fig. 11).

3.3. Sensitivity study of static material properties

The fatigue cohesive zone model requires the quasi-static fracture properties and a few fatigue-related parameters. However, strength
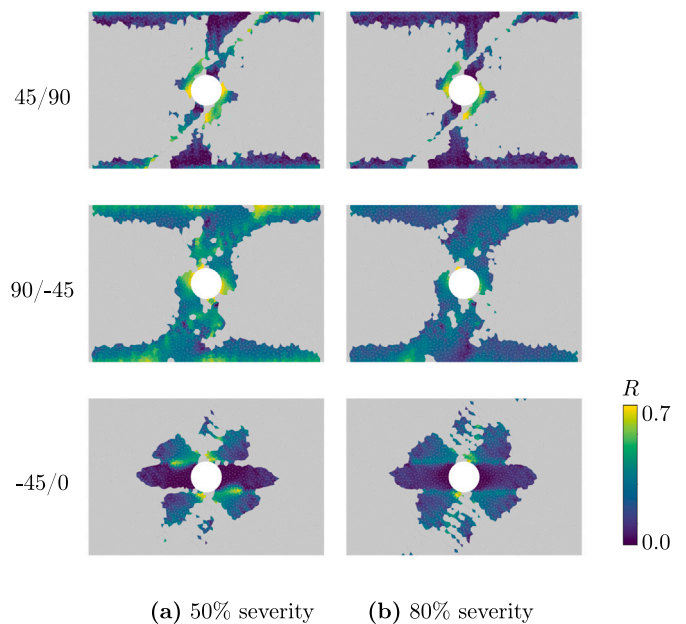

(a) 50% severity   **(b)** 80% severity

Fig. 12. *Local* stress ratio field in the cohesive zone for each interface at approximately 7% stiffness loss.
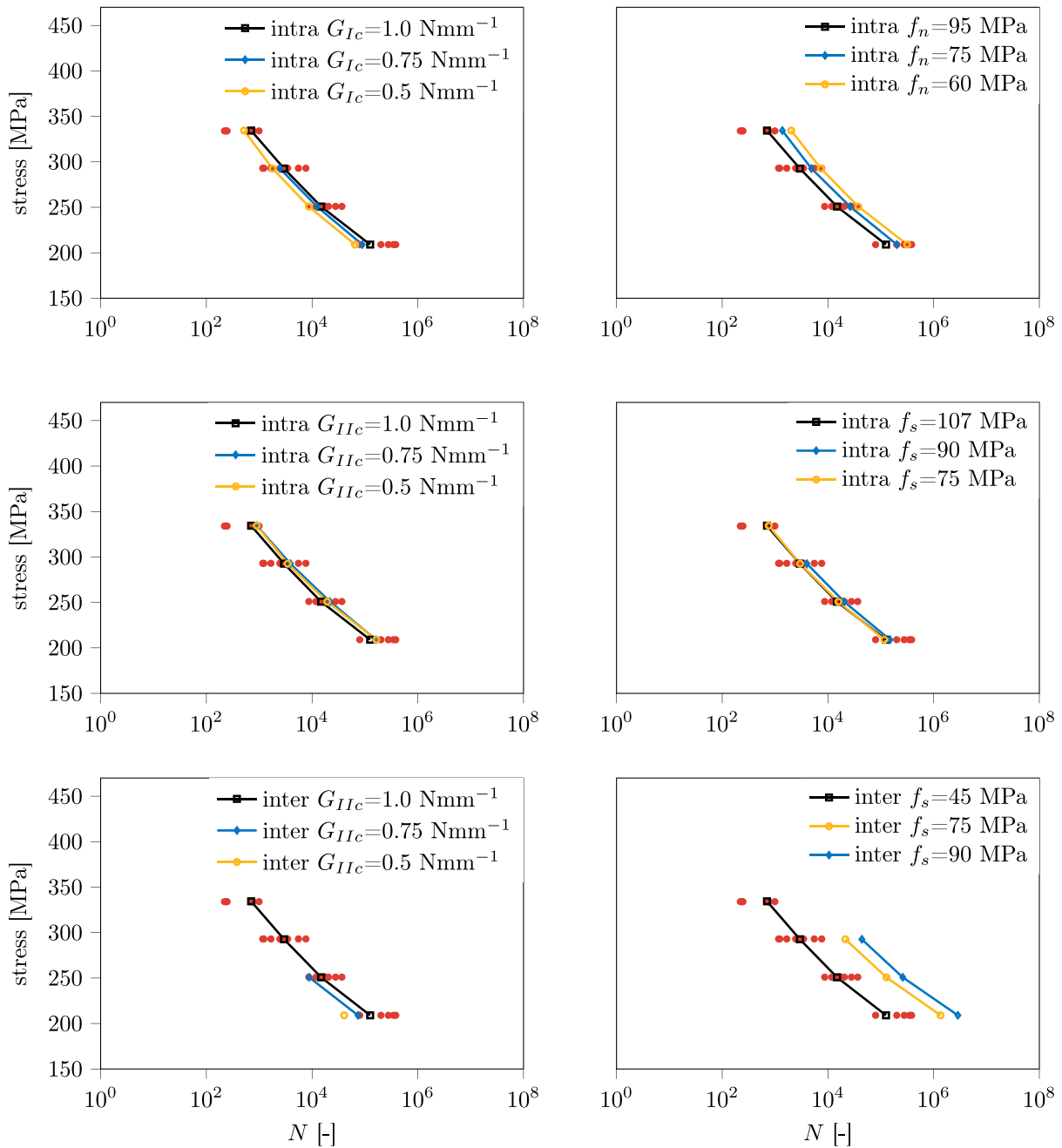
Fig. 13. Sensitivity study of static material properties.

measurements of IM7/8552 carbon fiber/epoxy vary with different testing methods [55,56]. Moreover, the strength measured with unidirectional laminates is smaller than the in-situ strength of embedded plies in a multidirectional laminate and depends on the fiber direction in the constraining plies, the ply thickness and the location of ply in the laminate [57–60].

The effect of the static fracture properties on the quasi-isotropic laminate simulations is investigated by repeating the simulation of the *base* case with properties tabulated in Table 1, changing one material property at a time. The effect of varying each static property on the laminate S-N curve is shown in Fig. 13.[2] The curve corresponding to the *base* case is indicated with the black line. It can be observed

that the response is only slightly affected by varying the intra-laminar fracture properties. The tensile strength seems to have the largest influence, where increasing the strength results in a shorter fatigue life. Decreasing the intra-laminar strength shifts the underlying *local* S-N curve downwards and consequently leads to more accumulated fatigue damage in the transverse matrix cracks. With more distributed intra-laminar cracking, tractions in the interface decrease and therefore less inter-laminar fatigue damage accumulates [35]. Since the largest stiffness drops are associated with interface delamination (see Fig. 7), the fatigue life of the laminate is longer. The interface shear strength shows the most influence on the *global* S-N curve, where an increase in shear strength results in a longer fatigue life. The slope of the underlying *local* S-N curve remains the same with increasing strength, while the curve is shifted upwards, thus resulting in less fatigue damage at the same stress level compared to a lower interfacial strength. Finally, decreasing the interfacial mode-II fracture energy results in a shorter fatigue life,
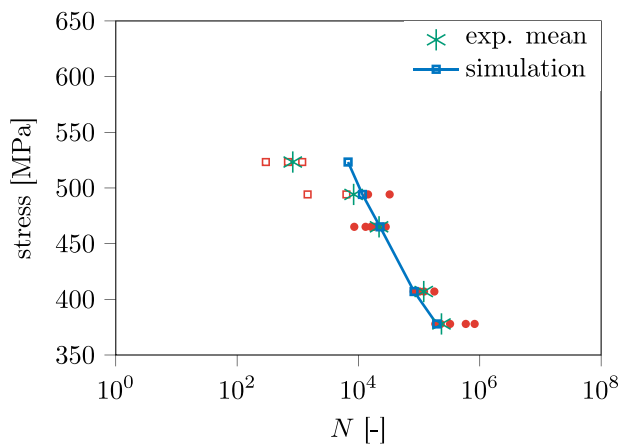
---

[2] Some simulations did not reach a 15% reduction in effective stiffness due to convergence issues, resulting in incomplete S-N plots.

Fig. 14. S-N curve of the sub-laminate scaled specimen. Experimental values are extracted from [16]. The symbols □ and • indicate experimental specimens with pull-out and delamination-type failure modes, respectively.

although the effect is minimal in the range of typical values for the mode-II fracture energy (0.75–1.0 N mm^{-1}).

Previously, the static version of the open-hole simulation [53] indicated that fracture energy is a more important parameter than strength, since laminate failure is governed by delamination propagation. In elementary static crack propagation tests, Turon's static mixed-mode cohesive zone model, which is the basis of the fatigue formulation by Dávila [26], ensures correct energy dissipation, independent of strength [39,40]. However, with the fatigue damage extension, it has been shown that crack propagation rates do in fact depend on the static strength values [29,61]. The results of the present study confirm these previous findings.

3.3.1. Sub-laminate scaled specimen

The *sub-laminate scaled specimen* is simulated with five maximum *global* stress levels $\sigma^{\max}$(MPa) = {523.3, 494.2, 465.1, 407.0, 377.9}, corresponding to 90, 85, 80, 70 and 65% severity levels, respectively. The *global* load ratio R_{glob} is 0.1.

The S-N curve is shown in Fig. 14, where fatigue life is again defined as the number of cycles to reach a 15% reduction of the initial effective stiffness. It can be observed that a good match is obtained in terms of fatigue life, except for the experimental specimens with the highest peak load. It is reported in Ref. [16] that the highest load level (90% severity) resulted in a pull-out failure mode (which cannot be captured with the present numerical framework where fiber failure is not considered), while the second highest load level (85% severity) showed both delamination and pull-out failures. However, the three lowest load levels resulted in all cases in a delamination-type failure mode in the experiments. For the specimens with a delamination-type failure mode, the simulation results are in excellent accordance with the experiments.

The simulation damage patterns are compared to the experimental patterns under severity 80%, at approximately 9% stiffness loss (see Fig. 15). The patterns are in good agreement for the outer 45/90, 90/ − 45 and inner 45/90 interfaces. Similar to the experimental observations [16,20], damage grows from the free edge towards the hole in the inner 45/90 interface. Also a more dispersed damage pattern compared to the *ply-level scaled specimen*, with increased free-edge delamination, can be observed. For the outer −45/0 and 0/45 interfaces, slightly underdeveloped delamination is predicted, while the inner −45/0 interface shows overdeveloped delamination. Given the scatter in experimental damage patterns [16,20], the simulated patterns are overall in good correspondence with the experimental ones.

4. Conclusion

A previously developed progressive fatigue failure framework has been extended with an adaptive cycle jump approach to capture non-uniform local stress ratios in multidirectional laminates with thermal residual stresses. The local stress ratio is regularly computed by explicitly applying a load cycle to assess the minimum and maximum stress in every integration point, before cycle jumps take place.

The progressive fatigue failure framework is applied to the simulation of two open-hole quasi-isotropic laminates. The model is capable of predicting the fatigue life as a consequence of interacting intra- and inter-laminar damage with excellent agreement. Furthermore, the experimentally observed damage evolution and final failure modes are accurately captured. Moreover, the implicit fatigue damage update, together with the adaptive stepping scheme, allows for simulating a large amount of fatigue cycles while accounting for local stress ratios in an efficient manner. In addition, it is demonstrated that computing the local stress ratios, instead of just using the global load ratio, is relevant for this type of problems.

The numerical model requires only static material properties and a few fatigue-related parameters, calibrated on elementary fracture tests. Static parameters were taken from earlier simulations of static open-hole experiments, including adaptations for improved robustness. The effect of local stress ratio and mode-mixity is internally accounted for in the constitutive relations of the fatigue cohesive zone model, which poses a significant advantage over Paris-type models that require Paris data for different mode-mixities and stress ratios and separate S-N curves for crack initiation. However, the progressive fatigue failure model shows sensitivity to the static material properties, in particular to the inter-laminar strength. Previously it has been shown, with the static version of the open-hole tests, that fracture energy is a more important parameter than strength. Conversely, the present investigation indicates that static strength is an important parameter in the fatigue simulations with the embedded fatigue cohesive zone model.

The progressive fatigue failure framework has been validated for the case of multidirectional laminates with complex failure processes and thermal residual stresses, demonstrating an important step towards efficient virtual testing of composite structural elements under high-cycle fatigue loading.

CRediT authorship contribution statement

P. Hofman: Writing – original draft, Visualization, Software, Methodology, Conceptualization. **F.P. van der Meer:** Writing – review & editing, Supervision, Methodology, Funding acquisition, Conceptualization. **L.J. Sluys:** Writing – review & editing, Supervision, Methodology, Funding acquisition.

Declaration of competing interest

The authors declare that they have no known competing financial interests or personal relationships that could have appeared to influence the work reported in this paper.

Data availability

Data presented in this article is available at the 4TU. Research-Data repository throughhttps://doi.org/10.4121/27882b00-c605-4ad6-a09d-502bc9d69795.
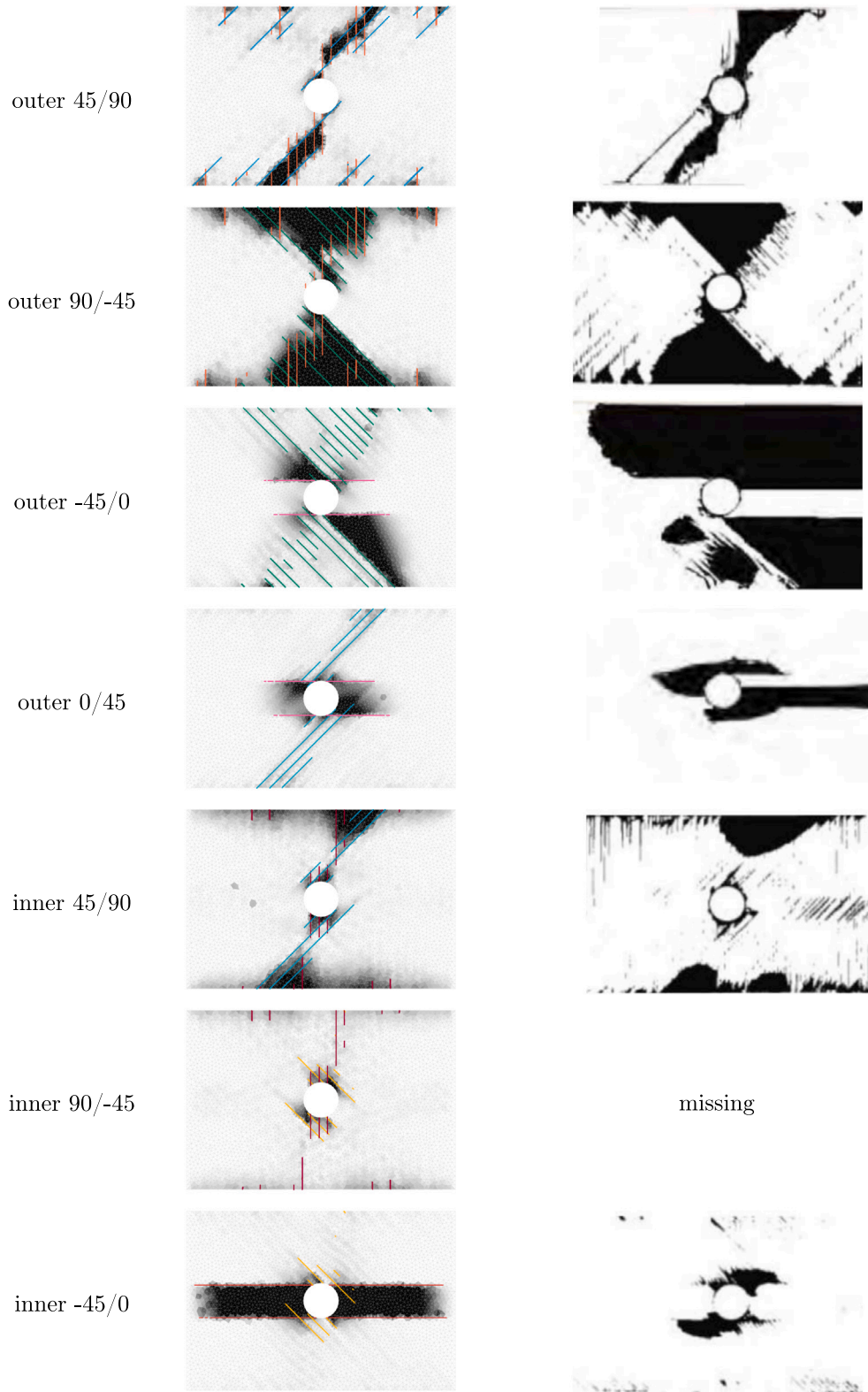
Acknowledgment

Fig. 15. Sub-laminate scaled specimen: damage in XFEM matrix cracks and interface delamination vs experimental CT scans (taken from [20]) at 9% stiffness loss. Only fully damaged matrix cracks ($D = 1$) are depicted.

References

[1] Peerlings RHJ, Brekelmans WAM, de Borst R, Geers MGD. Gradient-enhanced damage modelling of high-cycle fatigue. Internat J Numer Methods Engrg 2000;49:1547–69. http://dx.doi.org/10.1002/1097-0207(20001230)49:12<1547::AID-NME16>3.0.CO;2-D.

[2] Turon A, Costa J, Camanho P, Dávila C. Simulation of delamination in composites under high-cycle fatigue. Composites A 2007;38(11):2270–82. http://dx.doi.org/10.1016/j.compositesa.2006.11.009.

[3] Harper PW, Hallett SR. A fatigue degradation law for cohesive interface elements – Development and application to composite materials. Int J Fatigue 2010;32(11):1774–87. http://dx.doi.org/10.1016/j.ijfatigue.2010.04.006.

[4] Kawashita LF, Hallett SR. A crack tip tracking algorithm for cohesive interface element analysis of fatigue delamination propagation in composite materials. Int J Solids Struct 2012;49(21):2898–913. http://dx.doi.org/10.1016/j.ijsolstr.2012.03.034.

[5] Latifi M, van der Meer FP, Sluys LJ. A level set model for simulating fatigue-driven delamination in composites. Int J Fatigue 2015;80:434–42. http://dx.doi.org/10.1016/j.ijfatigue.2015.07.003.

[6] Bak B, Turon A, Lindgaard A, Lund E. A simulation method for high-cycle fatigue-driven delamination using a cohesive zone model. Internat J Numer Methods Engrg 2016. http://dx.doi.org/10.1002/nme.5117.

[7] Latifi M, van der Meer FP, Sluys LJ. Fatigue modeling in composites with the thick level set interface method. Composites A 2017;101:72–80. http://dx.doi.org/10.1016/j.compositesa.2017.05.035.

[8] Latifi M, van der Meer FP, Sluys LJ. An interface thick level set model for simulating delamination in composites. Internat J Numer Methods Engrg 2017;111(4):303–24. http://dx.doi.org/10.1002/nme.5463.

[9] Amiri-Rad A, Mashayekhi M. A cohesive zone approach for fatigue-driven delamination analysis in composite materials. Appl Compos Mater 2017;24(4):751–69. http://dx.doi.org/10.1007/s10443-016-9543-y.

[10] Amiri-Rad A, Mashayekhi M, van der Meer FP. Cohesive zone and level set method for simulation of high cycle fatigue delamination in composite materials. Compos Struct 2017;160:61–9. http://dx.doi.org/10.1016/j.compstruct.2016.10.041.

[11] Latifi M, Kouchakzadeh MA. Modeling the R-curve effects in laminate composites using the interface thick level set method. Theor Appl Fract Mech 2020;108. http://dx.doi.org/10.1016/j.tafmec.2020.102645.

[12] Carreras L, Turon A, Bak BL, Lindgaard E, Renart J, Martin de la Escalera F, et al. A simulation method for fatigue-driven delamination in layered structures involving non-negligible fracture process zones and arbitrarily shaped crack fronts. Composites A 2019;122:107–19. http://dx.doi.org/10.1016/j.compositesa.2019.04.026.

[13] Trabal GG, Bak BLV, Chen B, Carreras L, Lindgaard E. An adaptive floating node based formulation for the analysis of multiple delaminations under high cycle fatigue loading. Composites A 2022;160:107036. http://dx.doi.org/10.1016/j.compositesa.2022.107036.

[14] Spearing SM, Beaumont PW. Fatigue damage mechanics of composite materials. I: Experimental measurement of damage and post-fatigue properties. Compos Sci Technol 1992;44(2):159–68. http://dx.doi.org/10.1016/0266-3538(92)90109-G.

[15] Nixon-Pearson OJ, Hallett SR, Withers PJ, Rouse J. Damage development in open-hole composite specimens in fatigue. Part 1: Experimental investigation. Compos Struct 2013;106:882–9. http://dx.doi.org/10.1016/j.compstruct.2013.05.033.

[16] Nixon-Pearson OJ, Hallett SR. An investigation into the damage development and residual strengths of open-hole specimens in fatigue. Composites A 2015;69:266–78. http://dx.doi.org/10.1016/j.compositesa.2014.11.013.

[17] Aymerich F, Found MS. Response of notched carbon/PEEK and carbon/epoxy laminates subjected to tension fatigue loading. Fatigue Fract Eng Mater Struct 2000;23(8):675–83. http://dx.doi.org/10.1046/j.1460-2695.2000.00262.x.

[18] Nixon-Pearson OJ, Hallett SR, Harper PW, Kawashita LF. Damage development in open-hole composite specimens in fatigue. Part 2: Numerical modelling. Compos Struct 2013;106:890–8. http://dx.doi.org/10.1016/j.compstruct.2013.05.019.

[19] Iarve EV, Hoos K, Braginsky M, Zhou E, Mollenhauer DH. Progressive failure simulation in laminated composites under fatigue loading by using discrete damage modeling. J Compos Mater 2016;51(15):2143–61. http://dx.doi.org/10.1177/0021998316681831.

[20] Tao C, Mukhopadhyay S, Zhang B, Kawashita LF, Qiu J, Hallett SR. An improved delamination fatigue cohesive interface model for complex three-dimensional multi-interface cases. Composites A 2018;107:633–46. http://dx.doi.org/10.1016/j.compositesa.2018.02.008.

[21] Zheng T, Guo L, Wang Z, Benedictus R, Pascoe J-A. A reliable progressive fatigue damage model for life prediction of composite laminates incorporating an adaptive cyclic jump algorithm. Compos Sci Technol 2022;227:109587. http://dx.doi.org/10.1016/j.compscitech.2022.109587.

[22] Lu W-T, Gao Z, Adluru HK, Hoos KH, Seneviratne WP, Mollenhauer DH, et al. Fatigue damage modeling in laminated composite by using Rx-FEM and strength tracking method. Composites A 2022;163:107199. http://dx.doi.org/10.1016/j.compositesa.2022.107199.

[23] Tao C, Zhang C, Ji H, Qiu J. A Paris-law-informed neural fatigue cohesive model and its application to open-hole composite laminates. Int J Solids Struct 2023;267:112158. http://dx.doi.org/10.1016/j.ijsolstr.2023.112158.

[24] Llobet J, Maimí P, Turon A, Bak B, Lindgaard E, Carreras L, et al. A continuum damage model for composite laminates: Part IV- Experimental and numerical tests. Mech Mater 2021;154:103686. http://dx.doi.org/10.1016/j.mechmat.2020.103686.

[25] Maneval V, Vedvik N-P, Echtermeyer AT. Progressive fatigue modelling of open-hole glass-fibre epoxy laminates. J Compos Sci 2023;7(12):516. http://dx.doi.org/10.3390/jcs7120516.

[26] Dávila CG. From S-N to the Paris law with a new mixed-mode cohesive fatigue model for delamination in composites. Theor Appl Fract Mech 2020;106:102499. http://dx.doi.org/10.1016/j.tafmec.2020.102499.

[27] Dávila CG, Rose CA, Murri GB, Jackson WC, Johnston WM. Evaluation of fatigue damage accumulation functions for delamination initiation and propagation. Nasa/Tp–2020-220584, 2020.

[28] Dávila CG. From S-N to the Paris law with a new mixed-mode cohesive fatigue model. NASA/TP–2018-219838, 2018.

[29] Leciñana I, Zurbitu J, Renart J, Turon A. A robust fatigue parameter determination method for a local fatigue Cohesive Zone Model. Int J Fatigue 2023;107582. http://dx.doi.org/10.1016/j.ijfatigue.2023.107582.

[30] Dávila CG, Joosten MW. A cohesive fatigue model for composite delamination based on a new material characterization procedure for the Paris law. Eng Fract Mech 2023;284:109232. http://dx.doi.org/10.1016/j.engfracmech.2023.109232.

[31] Leciñana I, Renart J, Turon A, Zurbitu J, Tijs B. Characterization and analysis of the mode I interlaminar fatigue behaviour of thermoplastic composites considering R-curve effects. Eng Fract Mech 2023;109273. http://dx.doi.org/10.1016/j.engfracmech.2023.109273.

[32] Raimondo A, Dávila CG, Bisagni C. Cohesive analysis of a 3D benchmark for delamination growth under quasi-static and fatigue loading conditions. Fatigue Fract Eng Mater Struct 2022. http://dx.doi.org/10.1111/FFE.13712.

[33] Liang YJ, Dávila CG, Iarve EV. A reduced-input cohesive zone model with regularized extended finite element method for fatigue analysis of laminated composites in Abaqus. Compos Struct 2021;275(April):114494. http://dx.doi.org/10.1016/j.compstruct.2021.114494.

[34] Joosten MW, Dávila CG, Yang Q. Predicting fatigue damage in composites subjected to general loading conditions. Composites A 2022;156:106862. http://dx.doi.org/10.1016/j.compositesa.2022.106862.

[35] Hofman P, van der Meer FP, Sluys LJ. A numerical framework for simulating progressive failure in composite laminates under high-cycle fatigue loading. Eng Fract Mech 2024;295:109786. http://dx.doi.org/10.1016/j.engfracmech.2023.109786.

[36] van der Meer FP, Sluys LJ. A phantom node formulation with mixed mode cohesive law for splitting in laminates. Int J Fract 2009;158(2):107–24. http://dx.doi.org/10.1007/s10704-009-9344-5.

[37] van der Meer FP, Sluys LJ. Mesh-independent modeling of both distributed and discrete matrix cracking in interaction with delamination in composites. Eng Fract Mech 2010;77(4):719–35. http://dx.doi.org/10.1016/j.engfracmech.2009.11.010.

[38] Turon A, Camanho PP, Costa J, Dávila CG. A damage model for the simulation of delamination in advanced composites under variable-mode loading. Mech Mater 2006;38(11):1072–89. http://dx.doi.org/10.1016/j.mechmat.2005.10.003.

[39] Turon A, Camanho PP, Costa J, Renart J. Accurate simulation of delamination growth under mixed-mode loading using cohesive elements: Definition of interlaminar strengths and elastic stiffness. Compos Struct 2010;92(8):1857–64. http://dx.doi.org/10.1016/j.compstruct.2010.01.012.

[40] Turon A, González EV, Sarrado C, Guillamet G, Maimí P. Accurate simulation of delamination under mixed-mode loading using a cohesive model with a mode-dependent penalty stiffness. Compos Struct 2018;184(October 2017):506–11. http://dx.doi.org/10.1016/j.compstruct.2017.10.017.

[41] Juvinall RC, Marshek KM. Fundamentals of machine component design. 5th ed. Hoboken, NJ: John Wiley & Sons; 2012.

[42] Hansbo A, Hansbo P. A finite element method for the simulation of strong and weak discontinuities in solid mechanics. Comput Methods Appl Mech Engrg 2004;193(33–35):3523–40. http://dx.doi.org/10.1016/j.cma.2003.12.041.

[43] van der Meer FP. Mesolevel modeling of failure in composite laminates: Constitutive, kinematic and algorithmic aspects. Arch Comput Methods Eng 2012;19(3):381–425. http://dx.doi.org/10.1007/s11831-012-9076-y.

[44] May M, Hallett SR. A combined model for initiation and propagation of damage under fatigue loading for cohesive interface elements. Composites A 2010;41(12):1787–96. http://dx.doi.org/10.1016/j.compositesa.2010.08.015.

[45] May M, Pullin R, Eaton M, Featherston C, Hallett SR. An advanced model for initiation and propagation of damage under fatigue loading - Part II: Matrix cracking validation cases. Compos Struct 2011;93(9):2350–7. http://dx.doi.org/10.1016/j.compstruct.2011.03.023.

[46] Raimondo A, Bisagni C. Analysis of local stress ratio for delamination in composites under fatigue loads. AIAA J 2020;58(1):455–63. http://dx.doi.org/10.2514/1.J058465.

[47] Van Paepegem W, Degrieck J, De Baets P. Finite element approach for modelling fatigue damage in fibre-reinforced composite materials. Composites B 2001;32(7):575–88. http://dx.doi.org/10.1016/S1359-8368(01)00038-5.

[48] Nojavan S, Schesser D, Yang QD. A two-dimensional in situ fatigue cohesive zone model for crack propagation in composites under cyclic loading. Int J Fatigue 2016;82:449–61. http://dx.doi.org/10.1016/j.ijfatigue.2015.08.029.

[49] Nojavan S, Schesser D, Yang QD. An in situ fatigue-CZM for unified crack initiation and propagation in composites under cyclic loading. Compos Struct 2016;146:34–49. http://dx.doi.org/10.1016/j.compstruct.2016.02.060.

[50] Sally O, Laurin F, Julien C, Desmorat R, Bouillon F. An efficient computational strategy of cycle-jumps dedicated to fatigue of composite structures. Int J Fatigue 2020;135:105500. http://dx.doi.org/10.1016/j.ijfatigue.2020.105500.

[51] Wells GN, Sluys LJ. A new method for modelling cohesive cracks using finite elements. Internat J Numer Methods Engrg 2001;50(12):2667–82. http://dx.doi.org/10.1002/nme.143.

[52] Jiang W-G, Hallett SR, Green BG, Wisnom MR. A concise interface constitutive law for analysis of delamination and splitting in composite materials and its application to scaled notched tensile specimens. Internat J Numer Methods Engrg 2007;69(9):1982–95. http://dx.doi.org/10.1002/nme.1842.

[53] van der Meer FP, Sluys LJ, Hallett SR, Wisnom MR. Computational modeling of complex failure mechanisms in laminates. J Compos Mater 2012;46(5):603–23. http://dx.doi.org/10.1177/0021998311410473.

[54] Green B, Wisnom M, Hallett S. An experimental investigation into the tensile strength scaling of notched composites. Composites A 2007;38(3):867–78. http://dx.doi.org/10.1016/j.compositesa.2006.07.008.

[55] Arndt CM, de Carvalho NV, Czabaj MW. Experimental reexamination of transverse tensile strength for IM7/8552 tape-laminate composites. J Compos Mater 2020;54(23):3297–312. http://dx.doi.org/10.1177/0021998320914065.

[56] May M, Hallett SR. An assessment of through-thickness shear tests for initiation of fatigue failure. Composites A 2010;41(11):1570–8. http://dx.doi.org/10.1016/j.compositesa.2010.07.005.

[57] Dvorak GJ, Laws N. Analysis of progressive matrix cracking in composite laminates II. First ply failure. J Compos Mater 1987;21(4):309–29. http://dx.doi.org/10.1177/002199838702100402.

[58] Arteiro A, Catalanotti G, Melro A, Linde P, Camanho P. Micro-mechanical analysis of the in situ effect in polymer composite laminates. Compos Struct 2014;116:827–40. http://dx.doi.org/10.1016/j.compstruct.2014.06.014.

[59] Laux T, Gan KW, Dulieu-Barton JM, Thomsen OT. Ply thickness and fibre orientation effects in multidirectional composite laminates subjected to combined tension/compression and shear. Composites A 2020;133:105864. http://dx.doi.org/10.1016/j.compositesa.2020.105864.

[60] Sun Q, Zhou G, Tang H, Meng Z, Jain M, Su X, et al. In-situ effect in cross-ply laminates under various loading conditions analyzed with hybrid macro/microscale computational models. Compos Struct 2021;261:113592. http://dx.doi.org/10.1016/j.compstruct.2021.113592.

[61] Lecinana I, Zurbitu J, Renart J, Turon A, Carreras L. Global sensitivity analysis of an SN curve-based fatigue cohesive zone model and validation through a benchmark test, 20th Eur. In: Conf. compos. mater. ECCM20. 2022.